

A SINFONI view of the nuclear activity and circumnuclear star formation in NGC 4303

Rogemar A. Riffel,¹★ L. Colina,^{2,3} T. Storchi-Bergmann,⁴ J. Piqueras López,²
S. Arribas,^{2,3} R. Riffel,⁴ M. Pastoriza,⁴ Dinalva A. Sales,⁴ N. Z. Dametto,⁴
A. Labiano⁵ and R. I. Davies⁶

¹Departamento de Física, Centro de Ciências Naturais e Exatas, Universidade Federal de Santa Maria, Santa Maria, RS 97105-900, Brazil

²Centro de Astrobiología (CAB, CSIC-INTA), Carretera de Ajalvir, Torrejón de Ardoz, E-28850 Madrid, Spain

³ASTRO-UAM, Universidad Autónoma de Madrid (UAM), Unidad Asociada CSIC, E-28049 Madrid, Spain

⁴Departamento de Astronomia, Instituto de Física, Universidade Federal do Rio Grande do Sul, CP 15051, Porto Alegre, RS 91501-970, Brazil

⁵Institute for Astronomy, Department of Physics, ETH Zurich, CH-8093 Zurich, Switzerland

⁶Max-Planck-Institut für extraterrestrische Physik, Postfach 1312, D-85741 Garching, Germany

Accepted 2016 July 4. Received 2016 June 28; in original form 2015 November 20

ABSTRACT

We present new maps of emission-line flux distributions and kinematics in both ionized (traced by H I and [Fe II] lines) and molecular (H₂) gas of the inner 0.7 × 0.7 kpc² of the galaxy NGC 4303, with a spatial resolution 40–80 pc and velocity resolution 90–150 km s⁻¹ obtained from near-IR integral field spectroscopy using the Very Large Telescope instrument SINFONI. The most prominent feature is a 200–250 pc ring of circumnuclear star-forming regions. The emission from ionized and molecular gas shows distinct flux distributions: while the strongest H I and [Fe II] emission comes from regions in the west side of the ring (ages ~ 4 Myr), the H₂ emission is strongest at the nucleus and in the east side of the ring (ages > 10 Myr). We find that regions of enhanced hot H₂ emission are anti-correlated with those of enhanced [Fe II] and H I emission, which can be attributed to post-starburst regions that do not have ionizing photons anymore but still are hot enough (~2000 K) to excite the H₂ molecule. The line ratios are consistent with the presence of an active galactic nucleus at the nucleus. The youngest regions have stellar masses in the range 0.3–1.5 × 10⁵ M_⊙ and ionized and hot molecular gas masses of ~0.25–1.2 × 10⁴ M_⊙ and ~2.5–5 M_⊙, respectively. The stellar and gas velocity fields show a rotation pattern, with the gas presenting larger velocity amplitudes than the stars, with a deviation observed for the H₂ along the nuclear bar, where increased velocity dispersion is also observed, possibly associated with non-circular motions along the bar. The stars in the ring show smaller velocity dispersion than the surroundings, which can be attributed to a cooler dynamics due to their recent formation from cool gas.

Key words: galaxies: active – galaxies: individual: NGC 4303 – galaxies: ISM – infrared: galaxies.

1 INTRODUCTION

Star formation (SF) in the circumnuclear regions of galaxies and its connection with the existence of nuclear young stellar clusters and/or active galactic nuclei (AGN) have been the subject of many studies over the past several decades since early models invoking dynamical resonances in a rotating bar potential (Combes & Gerin 1985), bars within bars (Shlosman, Frank & Begelman 1989) and the direct feeding of AGN due to stellar winds or cloud–cloud collisions in the vicinity of the nucleus (Norman & Scoville 1988;

Shlosman, Begelman & Frank 1990). Some models (e.g. Heller & Shlosman 1994; Knapen et al. 1995) suggest that gas could flow inwards from the ring, creating a disc of gas that, if massive enough, would become unstable. Under this scenario, a massive black hole in the nucleus could be fed triggering an AGN (Shlosman et al. 1989 1989; Fukuda, Wada & Habe 1998).

Regarding SF in nuclear rings, two scenarios have been proposed: the ‘popcorn’ (Elmegreen 1994) and the ‘pearls on a string’ (Böker et al. 2008). The ‘popcorn’ scenario assumes that the cold molecular gas is accumulated in a circumnuclear resonance ring. If massive enough, the ring becomes gravitational unstable, fragmenting in clumps and forming stellar clusters at random positions. On the other hand, in the ‘pearls-on-a-string’ scenario, new

* E-mail: rogemar@ufsm.br

stars are exclusively formed in the regions where the gas enters the ring (i.e. the regions of maximum gas density). These young clusters evolve passively as they orbit along the ring, producing a string of ageing clusters. Independent of the formation mechanism of the stellar clusters, the role of these clusters as they move along the ring can be important. Stellar winds and subsequent supernova (SN) explosions can affect their surrounding interstellar medium, removing gas and halting subsequent SF, as well as generating shocks that will reduce the angular momentum of the gas, that could eventually fall towards the centre, feeding the AGN and/or forming a nuclear star cluster.

Detailed multi-wavelength two-dimensional spectroscopic studies in nearby galaxies with the adequate spatial resolution (~ 10 pc, or less) are needed to further investigate the evolutionary scenarios mentioned above. CO interferometric maps [Plateau de Bure interferometer (PdBI)] have shown the presence of a wide range of molecular gas structures in the central kpc region of nearby galaxies with an AGN (García-Burillo et al. 2005). According to these studies, most of the molecular gas is concentrated in the form of a circumnuclear ring of several hundred pc to kpc size, while ≈ 33 per cent of the galaxies show the evidence for a direct gas fuelling into the AGN down to scales of ~ 50 pc (García-Burillo & Combes 2012). Of particular importance, the near-infrared (near-IR) bands allow the study of the multi-phase gas, from molecular (H_2) to shocked partially ionized (Fe II) to highly ionized gas (e.g. Ca VIII), that can trace a number of different physical structures and mechanisms, from molecular gas reservoirs to AGN outflows.

In the near-IR, recent studies using integral field spectroscopy (IFS; Genzel et al. 1995) have been particularly useful to map the stellar and gas kinematics, as well as the gas excitation and distribution of the different gas phases (e.g. Barbosa et al. 2014; Riffel et al. 2014). In nearby Seyfert galaxies, compact (scales of few tens of parsecs) molecular gas discs (Hicks et al. 2009; Riffel & Storchi-Bergmann 2011; Mazzalay et al. 2014), streaming motions towards the nucleus (e.g. Davies et al. 2014; Diniz et al. 2015), ionized gas outflows (e.g. Storchi-Bergmann et al. 2010; Iserlohe et al. 2013) and young stellar populations (e.g. Davies et al. 2007) have been mapped in the nuclear regions. In addition, studies of circumnuclear star-forming rings (CNSFRs) at hundred of pc from the nucleus in nearby spirals (Böker et al. 2008; van der Laan et al. 2013a, 2015; Falcón-Barroso et al. 2014) have focused on establishing the reality of the proposed evolutionary scenarios for the star-forming rings, such as the ‘popcorn’ scenario (Elmegreen 1994) and the ‘pearls-on-a-string’ scenario (Böker et al. 2008).

All these previous studies have been focused on either nearby luminous Seyfert galaxies where the output energy is dominated by the AGN or galaxies with luminous CNSFRs. Here we perform a similar study for NGC 4303, a nearby galaxy with both a (low-luminosity) AGN and a star-forming ring, and that has also a young massive cluster at the nucleus. In addition, multi-wavelength observations (Colina et al. 1997, 2002; Colina & Arribas 1999) reveal a spiral of CNSFRs that can be traced all the way into the inner few parsecs (e.g. Colina & Wada 2000; Jiménez-Bailón et al. 2003), suggesting that it could be the feeding channel to the AGN and nuclear star cluster. Finally, a high-velocity nuclear outflow extending up to ≈ 120 pc to the north-east of the nucleus has also been observed in optical line emission of [O III] (Colina & Arribas 1999).

NGC 4303 is at a distance of 16.1 Mpc (Colina & Arribas 1999), and is classified as an SB(rs)bc (de Vaucouleurs et al. 1991). It is abundant in cold molecular gas (Schinnerer et al. 2002) that shows the global distribution expected for the gas flow in a strong, large-scale bar, and the two-arm spiral structure in the inner kiloparsec

can be explained by a density wave activated by the potential of that bar.

In this paper, we present near-IR IFS of the inner 350 pc radius of NGC 4303, obtained with the integral field spectrograph SINFONI at the Very Large Telescope (VLT) in order to map the kinematics and excitation properties of the different phases of the interstellar medium in the circumnuclear region. It is the first time that such mapping is provided in the near-IR. This work is organized as follows: Section 2 presents the observations and data reduction procedure, while in Section 3, we present maps for emission-line flux distributions and ratios, as well as for the gas and stellar kinematics. The results are discussed in Section 4, and Section 5 presents the conclusions of this work.

2 OBSERVATIONS AND DATA REDUCTION

The observations were done using the near-IR spectrograph SINFONI of the VLT, during the period 82B (February 2009). The pointings were centred on the nucleus of the galaxy, covering a field of view (FoV) of ~ 8 arcsec \times 8 arcsec per exposure, enlarged by dithering up to ~ 9.25 arcsec \times 9.25 arcsec, with a plate scale of 0.125×0.220 arcsec pixel $^{-1}$. This corresponds to an average coverage of $\sim 0.7 \times 0.7$ kpc with a spatial sampling of ~ 10 pc per pixel.

The data were taken in the J (1.10–1.35 μm), H (1.45–1.80 μm) and K (1.97–2.44 μm) bands with a total integration time of 2400 s per band. In the same way, a set of photometric standard stars was observed to perform the telluric and flux calibration. We estimated the spatial resolution of our seeing-limited observations by fitting a 2D Gaussian profile to a collapsed image of the standard stars. The spatial resolution (full width at half-maximum) measured for each band is ~ 1 , ~ 0.6 and ~ 0.5 arcsec for the J , H and K band, respectively, that correspond to 78, 47 and 39 pc at the adopted distance of 16.1 Mpc.

The reduction and calibration processes were performed using the standard ESO pipeline `ESOREX` (version 3.8.3), and our own `IDL` routines. The usual corrections of dark, flat-fielding, detector linearity, geometrical distortion and wavelength calibration were applied to each object and sky frames, before subtracting the sky emission from each on-source frame. After each individual data cube was calibrated, we constructed a final data cube per band, taking the relative shifts in the dithering pattern into account.

The calibration of each individual data cube was performed in two steps. First, we removed the telluric absorption from the spectra. We extracted the integrated spectrum of the corresponding standard star within an aperture of 3σ of the best 2D Gaussian fit of a collapsed image. We normalized the spectrum by a blackbody profile at the T_{eff} from the Tycho-2 Spectral Type Catalog (Wright et al. 2003), after removing the strongest absorption features of the stars. The result is a *sensitivity function* that accounts for the telluric absorption.

Secondly, each data cube was flux calibrated. The spectrum of the standard star was converted from counts to physical units using the response curves of the 2MASS filters (Cohen, Wheaton & Megeath 2003), and the J , H and K magnitudes from the 2MASS catalogue (Skrutskie et al. 2006). We then obtained a conversion factor from counts to physical units. Each individual data cube was then divided by its corresponding *sensitivity function* and multiplied by this conversion factor to obtain a full-calibrated data cube. The estimated uncertainty for the conversion factor is ≤ 15 per cent for each band.

After the data reduction procedure, we performed a spatial filtering of the data cubes using a Butterworth bandpass filter (e.g. Gonzalez & Woods 2002; Menezes, Steiner & Ricci 2015) in order

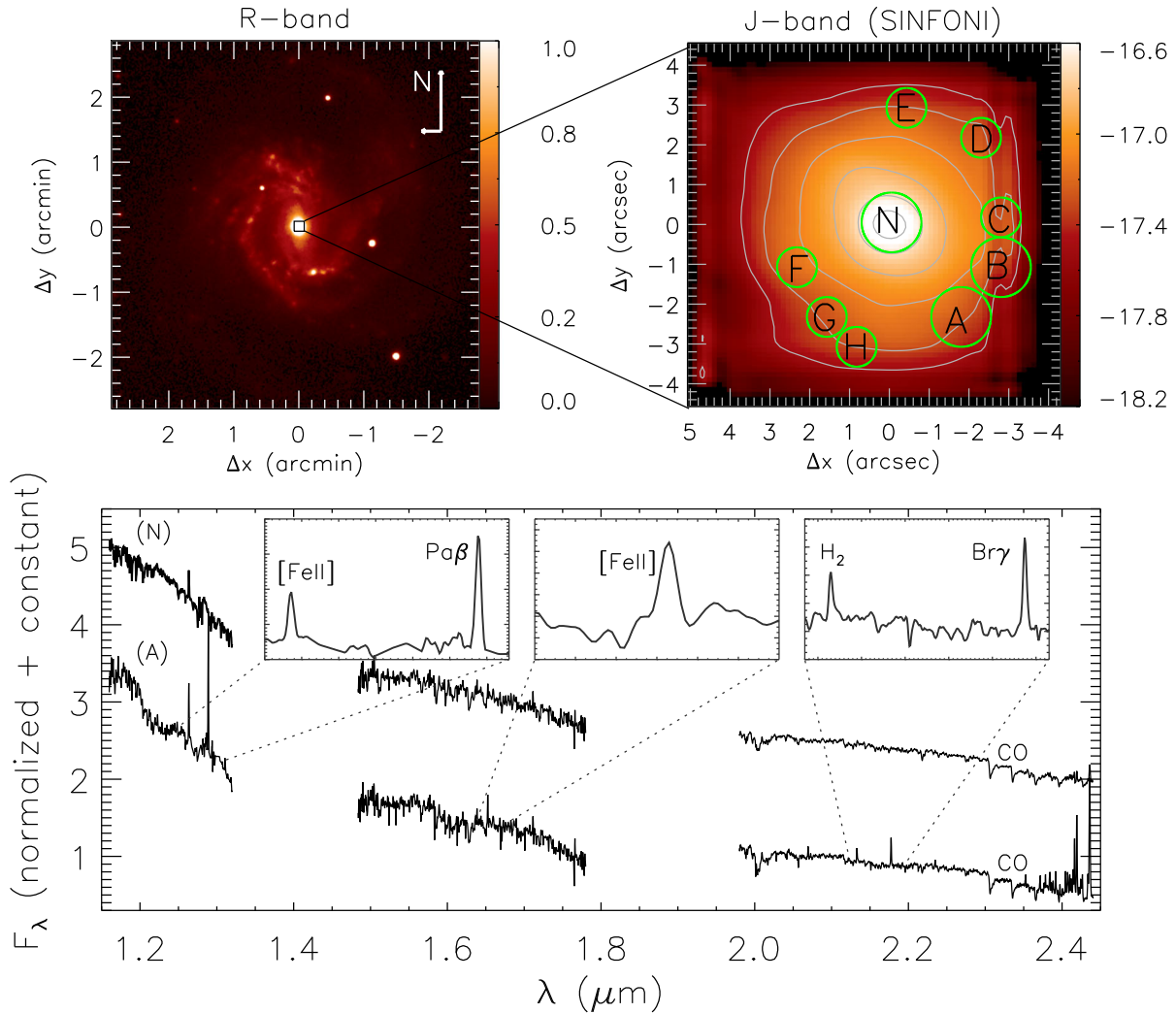


Figure 1. Large-scale image in the *R* band (top-left) from Koopmann, Kenney & Young (2001). *J*-band continuum, reconstructed from the SINFONI data cube as an average of the fluxes between 1.15 and 1.20 μm (top right). The circles mark the position of the CNSFRs and the bottom panel shows the near-IR spectra for the nucleus (top) and for position A (bottom), obtained for a circular aperture with radius 0.75 arcsec and normalized at 2.1 μm . The sub-panels present a zoom of the spectra from position A to better show the main emission lines. The *K*-band CO absorption band heads are clearly visible in both spectra. A constant (1.5) was added to the nuclear spectrum for visualization purpose. The colour bar for the large-scale image is in arbitrary units and for the *J* band it shows the fluxes in logarithmic units [$\log(\text{erg s}^{-1} \text{cm}^{-1} \text{spaxel}^{-1})$].

to remove noise from the observed cubes. The final signal-to-noise ratio (snr) in the continuum is in the range 3–10 for the *J* band with the smallest values observed close to the borders of the FoV and the highest values at the nucleus, while for the *H* and *K* bands we get $\text{snr} = 3\text{--}15$. The improvement of the snr by the spatial filtering ranges from 30 to 5 per cent, from the borders of the FoV to the nucleus for all bands, as obtained by calculating the ratios between the snr of the filtered cubes and those of the original ones. By comparing the continuum images for the original and filtered cubes, we concluded that the filtering procedure does not change the angular resolution of the data.

3 RESULTS

The top-left panel of Fig. 1 shows a large-scale optical image of NGC 4303 in the *R* band from Koopmann et al. (2001).¹ In the

¹This image is available at NASA/IPAC Extragalactic Database (<http://ned.ipac.caltech.edu>).

top-right panel, we show the *J*-band continuum image obtained from the SINFONI data cube for the inner $9 \times 9 \text{ arcsec}^2$, where we label the nucleus ‘N’ as well as several star-forming regions, in particular region ‘A’ (a bright circumnuclear $\text{Br}\gamma$ emitting clump), for which the spectra are shown in the bottom panels. The spectra were obtained by integrating the fluxes within a circular aperture of radius 0.75 arcsec and normalized to the flux at 2.1 μm . The two spectra show similar slopes, suggesting that the nuclear and extranuclear continuum emission have similar origins. On the other hand, the line emission is stronger in region ‘A’ than at the nucleus. In the bottom panel, we present also a zoom of spectrum from position A showing the main emission lines: $[\text{Fe II}] \lambda 1.64 \mu\text{m}$, $[\text{Fe II}] \lambda 1.25 \mu\text{m}$, $\text{Pa}\beta$, $\text{Br}\gamma$ and $\text{H}_2 \lambda 2.12 \mu\text{m}$.

3.1 Emission-line flux distributions and ratios

Different phases of the interstellar medium can be traced in the near-IR by distinct emission lines: ionized (traced by $\text{Br}\gamma$ and $\text{Pa}\beta$ lines),

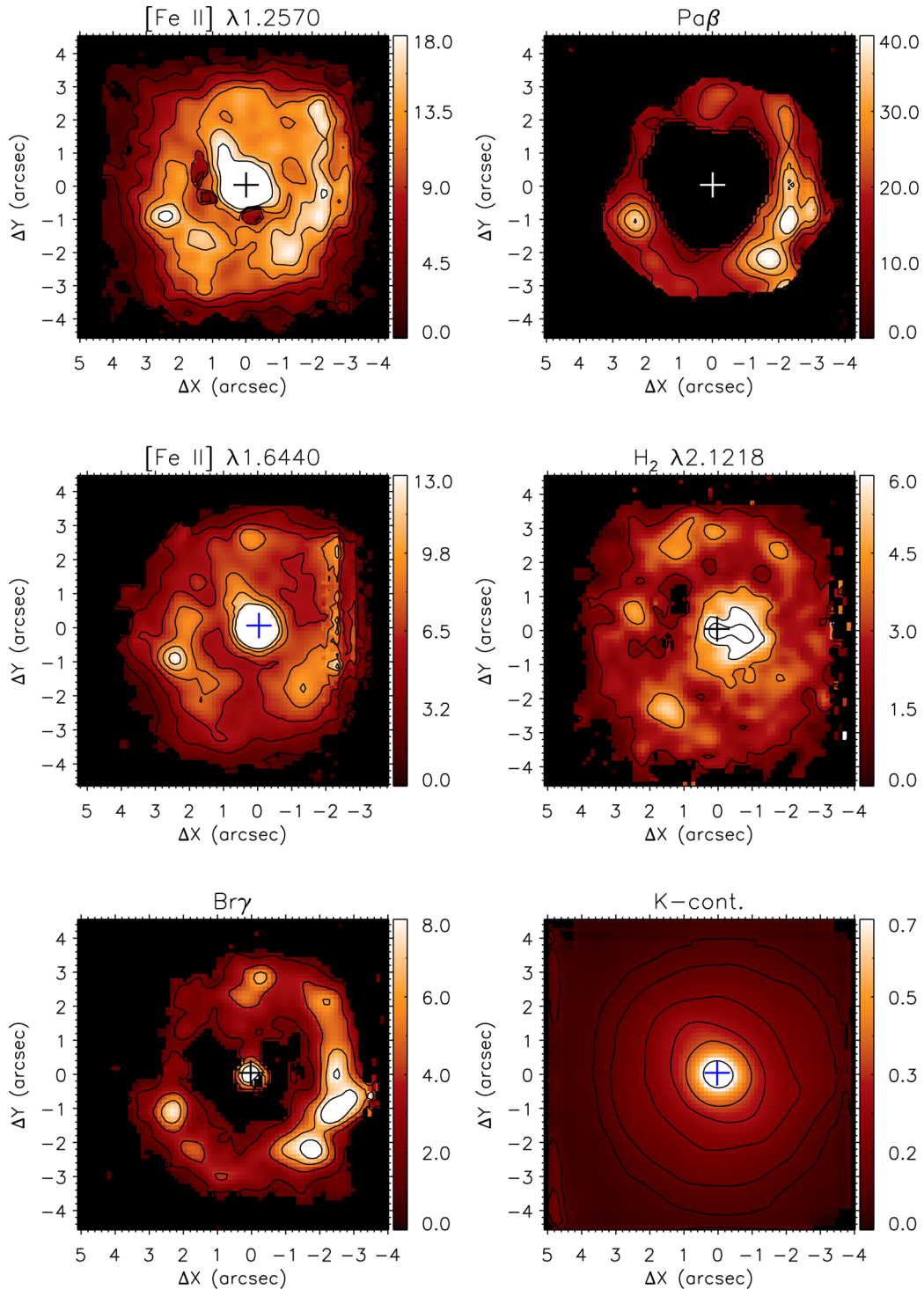


Figure 2. Emission-line flux distributions. The colour bars show the fluxes in units of $10^{-18} \text{ erg s}^{-1} \text{ cm}^{-2}$ and the central cross marks the position of the nucleus. Black locations are masked regions due to the non-detection of the emission lines or due to bad fits of their profiles.

partially ionized/shocks ($[\text{Fe II}]$ lines) and hot molecular gas (H_2 lines). We used the emission-line PROFILE FITTING (PROFIT) routine (Riffel 2010) to fit the line profiles with Gaussians and constructed maps for the flux distributions, centroid velocities and velocity dispersions for each emission line.

In Fig. 2, we show the flux distributions for the $[\text{Fe II}] \lambda 1.25 \mu\text{m}$, $\text{Pa}\beta$, $[\text{Fe II}] \lambda 1.64 \mu\text{m}$, $\text{H}_2 \lambda 2.12 \mu\text{m}$ and $\text{Br}\gamma$ emission lines. Black in these maps represent masked locations, where the snr of the lines

was not high enough to allow good fits, and regions where the lines were not detected. We masked regions with uncertainties in flux larger than 50 per cent, but, for most locations, the uncertainties are smaller than 20 per cent. The bottom-right panel shows the K -band continuum map. All emission lines present extended emission up to 4 arcsec ($\approx 300 \text{ pc}$), and the main feature of the flux distributions is a circumnuclear ring with clumps of enhanced line emission with radius in the range $\approx 2.5\text{--}3.2 \text{ arcsec}$ ($200\text{--}250 \text{ pc}$). Some differences

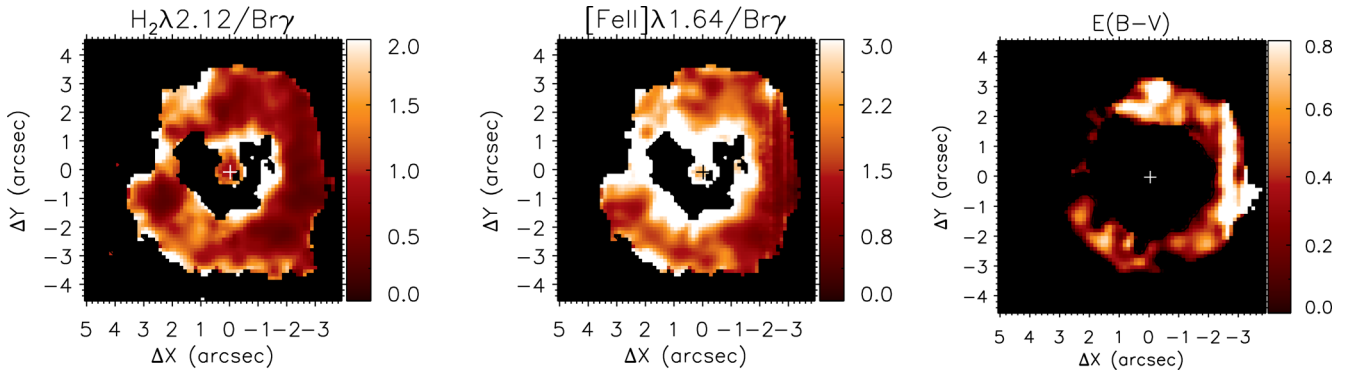


Figure 3. $\text{H}_2 \lambda 2.12 \mu\text{m}/\text{Br}\gamma$ and $[\text{Fe II}] \lambda 1.64 \mu\text{m}/\text{Br}\gamma$ emission-line ratios and reddening map. The central cross marks the position of the nucleus and black locations are masked regions due to the non-detection of the emission lines or due to bad fits of their profiles.

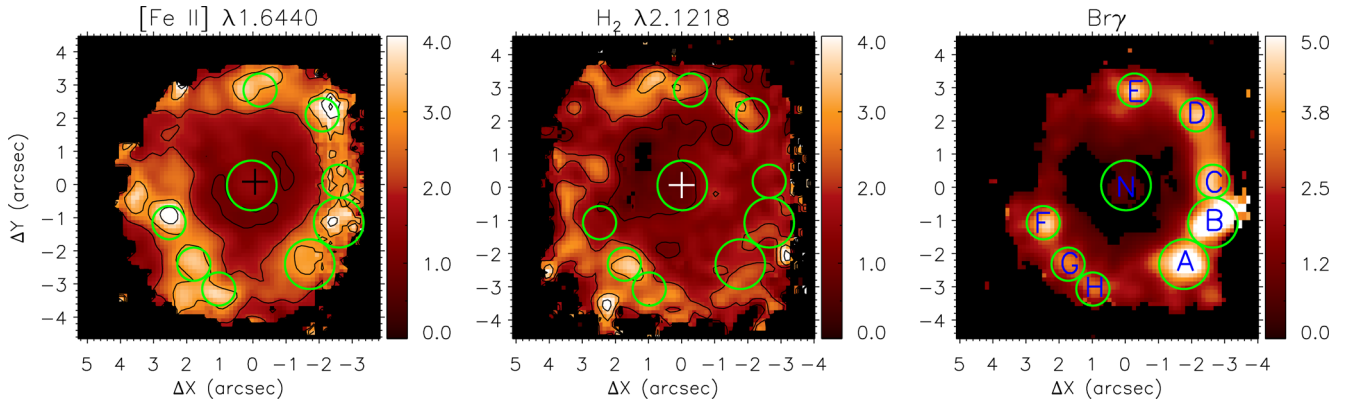


Figure 4. Equivalent width maps in \AA for the $[\text{Fe II}] \lambda 1.64 \mu\text{m}$, $\text{H}_2 \lambda 2.12 \mu\text{m}$ and $\text{Br}\gamma$ emission lines. The central cross marks the position of the nucleus and black locations are masked regions due to the non-detection of the emission lines or due to bad fits of their profiles. The circles in the $\text{Br}\gamma$ map show the regions used to extract the spectra of the CNSFRs and obtain the quantities listed in Table 1.

are observed among the distinct emission lines: (i) while the $[\text{Fe II}]$ and H_2 flux distributions present emission at the nucleus, $\text{Pa}\beta$ is not detected there, while $\text{Br}\gamma$ is marginally detected ($\text{snr} \approx 2$); (ii) along the ring, the H I and $[\text{Fe II}]$ emission is strongest to the west (including south-west), and at a region to the south-east, while the H_2 emission is strongest mostly to the east (including south-east and north-east).

In Fig. 3, we present the $\text{H}_2 \lambda 2.12 \mu\text{m}/\text{Br}\gamma$ and $[\text{Fe II}] \lambda 1.64 \mu\text{m}/\text{Br}\gamma$ emission-line ratio maps, useful to investigate the excitation mechanisms of the H_2 and $[\text{Fe II}]$ emission lines (e.g. Rounanen, Kotilainen & Prieto 2002; Rodríguez-Ardila et al. 2004; Rodríguez-Ardila, Riffel & Pastoriza 2005; Dors et al. 2012; Riffel et al. 2013a; Colina et al. 2015). Both ratios present the smallest values at the locations of the star-forming clumps in the circumnuclear ring. Larger values are seen between the ring and the nucleus, but the uncertainties are high due to low $\text{Br}\gamma$ emission. Typical values at the ring are $\text{H}_2 \lambda 2.12 \mu\text{m}/\text{Br}\gamma \sim 0.3$ and $[\text{Fe II}] \lambda 1.64 \mu\text{m}/\text{Br}\gamma \sim 0.7$, and, at the nucleus, ~ 1.4 and ~ 3 , respectively. A reddening map obtained from $\text{Pa}\beta/\text{Br}\gamma$ is shown in the right-hand panel of Fig. 3, with values ranging from 0 to 0.8, but most locations having values smaller than 0.4. As the extinction in the near-IR is thus small, the fluxes and flux ratios were not corrected for reddening.

Fig. 4 shows maps for the equivalent widths (EqWs) of the $[\text{Fe II}] \lambda 1.64$, $\text{H}_2 \lambda 2.12 \mu\text{m}$ and $\text{Br}\gamma$ emission lines. The highest values of EqW at the ring reach 5\AA for $\text{Br}\gamma$ and 4\AA for the H_2 and $[\text{Fe II}]$ emission lines. Several knots attributed to CNSFRs are clearly observed in the $\text{Br}\gamma$ EqW map which we used to extract the spectrum

for each region. The EqW values we have measured are low when compared with those expected for young (< 10 Myr) stellar populations, clearly indicating a large contribution of old stars to the near-IR continuum.

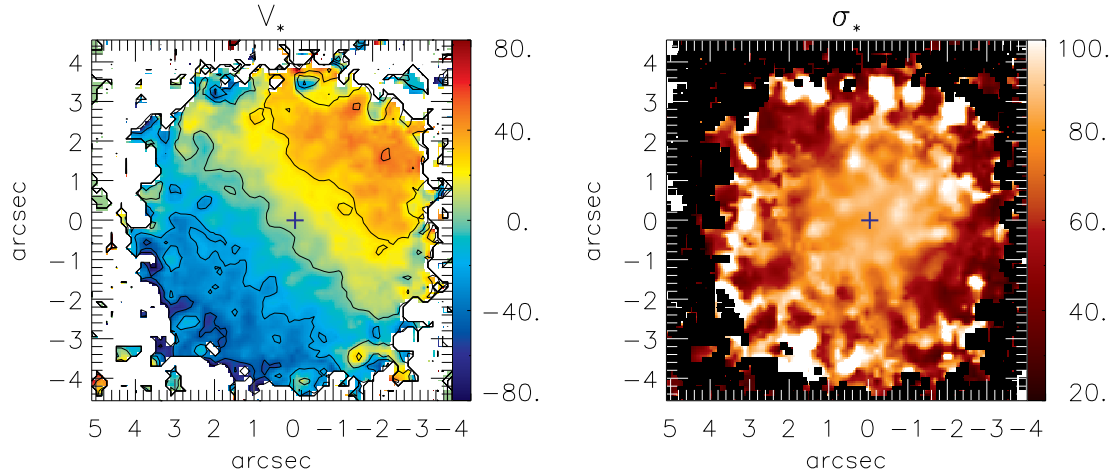
We have calculated the EqWs of the $\text{Br}\gamma$, $\text{Pa}\beta$, $[\text{Fe II}]$ and $\text{H}_2 \lambda 2.12 \mu\text{m}$ emission lines for regions labelled from A to F along the ring as well as for the nucleus and show their values, together with those of the emission-line fluxes in Table 1. The spectra of these regions were extracted within apertures of 0.75 arcsec for the nucleus and CNSFR A and 0.50 arcsec for the remaining regions. The apertures were chosen to be larger than the seeing and to include most of the $\text{Br}\gamma$ flux of each region.

3.2 Stellar and gas kinematics

We used the penalized pixel-fitting (pPXF) method of Cappellari & Emsellem (2004) to fit the CO absorption band heads at $2.3 \mu\text{m}$ and obtain the stellar velocity (V_*) field, velocity dispersion (σ_*) and higher order Gauss–Hermite moments (h_3 and h_4) as well as their uncertainties. We used the library of 60 stellar spectra of early-type stars from Winge, Riffel & Storchi-Bergmann (2009) as template spectra and fitted the galaxy spectra in the range from 2.29 to $2.41 \mu\text{m}$. The spectral resolution of the stellar spectra is better than the resolution of the galaxy spectra; thus, we degraded the template spectra to the same resolution of the SINFONI observations by convolving the spectra with a Gaussian function to get reliable σ_* measurements.

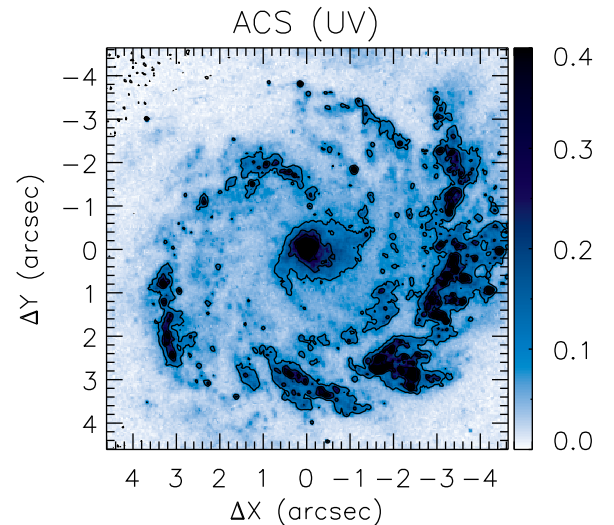
Table 1. Emission-line fluxes and equivalent widths for the CNSFRs in NGC 4303. Fluxes are shown in units of 10^{-16} erg s $^{-1}$ cm $^{-2}$ and the equivalent widths in Å.

Region	N	A	B	C	D	E	F	G	H
R	0.75 arcsec	0.75 arcsec	0.75 arcsec	0.50 arcsec					
$F_{\text{Br}\gamma}$	5.2 ± 3.7	7.1 ± 0.8	7.9 ± 1.0	3.3 ± 0.5	2.6 ± 0.5	2.4 ± 0.5	2.8 ± 0.5	1.9 ± 0.3	1.6 ± 0.4
$\text{EqW}_{\text{Br}\gamma}$	0.7 ± 0.5	4.4 ± 0.6	4.7 ± 0.7	4.0 ± 0.6	3.9 ± 0.8	3.5 ± 0.7	3.7 ± 0.7	2.9 ± 0.5	2.7 ± 0.7
$F_{\text{Pa}\beta}$	–	44.2 ± 8.9	42.6 ± 8.1	18.0 ± 3.8	15.7 ± 4.7	12.9 ± 4.7	17.7 ± 4.0	14.6 ± 4.1	14.5 ± 5.2
$\text{EqW}_{\text{Pa}\beta}$	–	12.3 ± 3.3	11.9 ± 3.3	9.5 ± 2.4	9.8 ± 3.3	8.2 ± 3.1	9.2 ± 2.4	9.8 ± 3.5	11.0 ± 4.8
$F_{[\text{Fe II}]1.64}$	18.9 ± 7.1	7.5 ± 1.7	7.1 ± 1.8	3.5 ± 1.2	4.3 ± 1.4	3.6 ± 1.3	4.7 ± 1.0	3.5 ± 0.8	2.9 ± 0.9
$\text{EqW}_{[\text{Fe II}]1.64}$	1.4 ± 0.5	3.0 ± 0.7	3.1 ± 0.9	3.0 ± 1.1	3.8 ± 1.4	3.2 ± 1.3	3.7 ± 1.0	3.3 ± 0.8	3.1 ± 1.1
$F_{[\text{Fe II}]1.25}$	34.3 ± 8.3	13.5 ± 2.2	12.6 ± 2.4	6.5 ± 1.4	7.2 ± 1.3	5.3 ± 1.4	7.7 ± 1.2	6.3 ± 0.9	5.6 ± 1.2
$\text{EqW}_{[\text{Fe II}]1.25}$	1.3 ± 0.3	3.0 ± 0.6	2.8 ± 0.7	2.8 ± 0.7	3.5 ± 0.9	2.7 ± 0.8	3.2 ± 0.7	3.3 ± 0.6	3.1 ± 0.8
$F_{\text{H}2.12}$	7.5 ± 3.6	3.5 ± 0.8	3.4 ± 0.7	1.5 ± 0.5	1.9 ± 0.4	1.8 ± 0.3	1.3 ± 0.4	2.2 ± 0.3	1.8 ± 0.4
$\text{EqW}_{\text{H}2.12}$	0.9 ± 0.4	2.1 ± 0.5	1.8 ± 0.4	1.8 ± 0.6	2.7 ± 0.6	2.4 ± 0.5	1.6 ± 0.5	3.1 ± 0.5	2.8 ± 0.6


Figure 5. Stellar velocity (V_*) field (left) and velocity dispersion (σ_*) map (right) obtained from the fit of the CO absorption band heads at 2.3 μm using the pPXF routine. The central cross marks the position of the nucleus and white/black locations in V_*/σ_* maps are masked regions due to bad fits of their profiles. The colour coded maps are given in units of km s^{-1} .

In Fig. 5, we present the stellar velocity field in the left-hand panel and the σ_* map in the right-hand panel. Black regions in these maps correspond to locations where the uncertainties in V_* and/or σ_* are larger than 30 km s^{-1} . The systemic velocity of the galaxy, derived in Section 4.3, was subtracted from the measured velocities and the colour bars are shown in units of km s^{-1} . The stellar velocity field is consistent with rotation in a disc with the major axis oriented along the position angle $\text{PA} \sim 135^\circ/315^\circ$ and with a projected (along the line of sight) velocity amplitude of about 70 km s^{-1} . The σ_* map shows values ranging from ~ 20 to $\sim 100 \text{ km s}^{-1}$, with the lowest values observed in a ring with radius of $\sim 2.5\text{--}3$ arcsec surrounding the nucleus, corresponding to the location of the CNSFRs. The largest σ_* values are observed in patchy regions that appear just beyond or surrounding the star-forming clumps, which we attribute to the velocity dispersions of the stellar bulge.

Fig. 6 presents the velocity fields and velocity dispersion (σ) maps for the $[\text{Fe II}]\lambda 1.64$, $\text{Br}\gamma$ and $\text{H}_2 \lambda 2.12 \mu\text{m}$ emission lines. We do not show the maps for the $[\text{Fe II}]\lambda 1.25$ and $\text{Pa}\beta$ emission lines because they are very similar to those for the $[\text{Fe II}]\lambda 1.64$ and $\text{Br}\gamma$ lines, respectively, and have lower snr. All velocity fields present a similar rotation pattern as seen for the stars with the orientation of the line of nodes ($\sim 130^\circ$) and the projected velocity amplitude (70 km s^{-1}) in good agreement with the values previously derived from the $\text{H}\beta$ emission line (Colina et al. 1997). The σ maps show small values over the whole FoV with the highest values reaching


Figure 6. Velocity (V) fields (left) and velocity dispersion (σ) maps (right) for the $[\text{Fe II}]\lambda 1.64 \mu\text{m}$ (top), $\text{H}_2 \lambda 2.12 \mu\text{m}$ (middle) and $\text{Br}\gamma$ emission lines. The central cross marks the position of the nucleus and white/black locations in V/σ maps are masked regions due to the non-detection of the emission lines or due to bad fits of their profiles. The colour bars are shown in units of km s^{-1} .

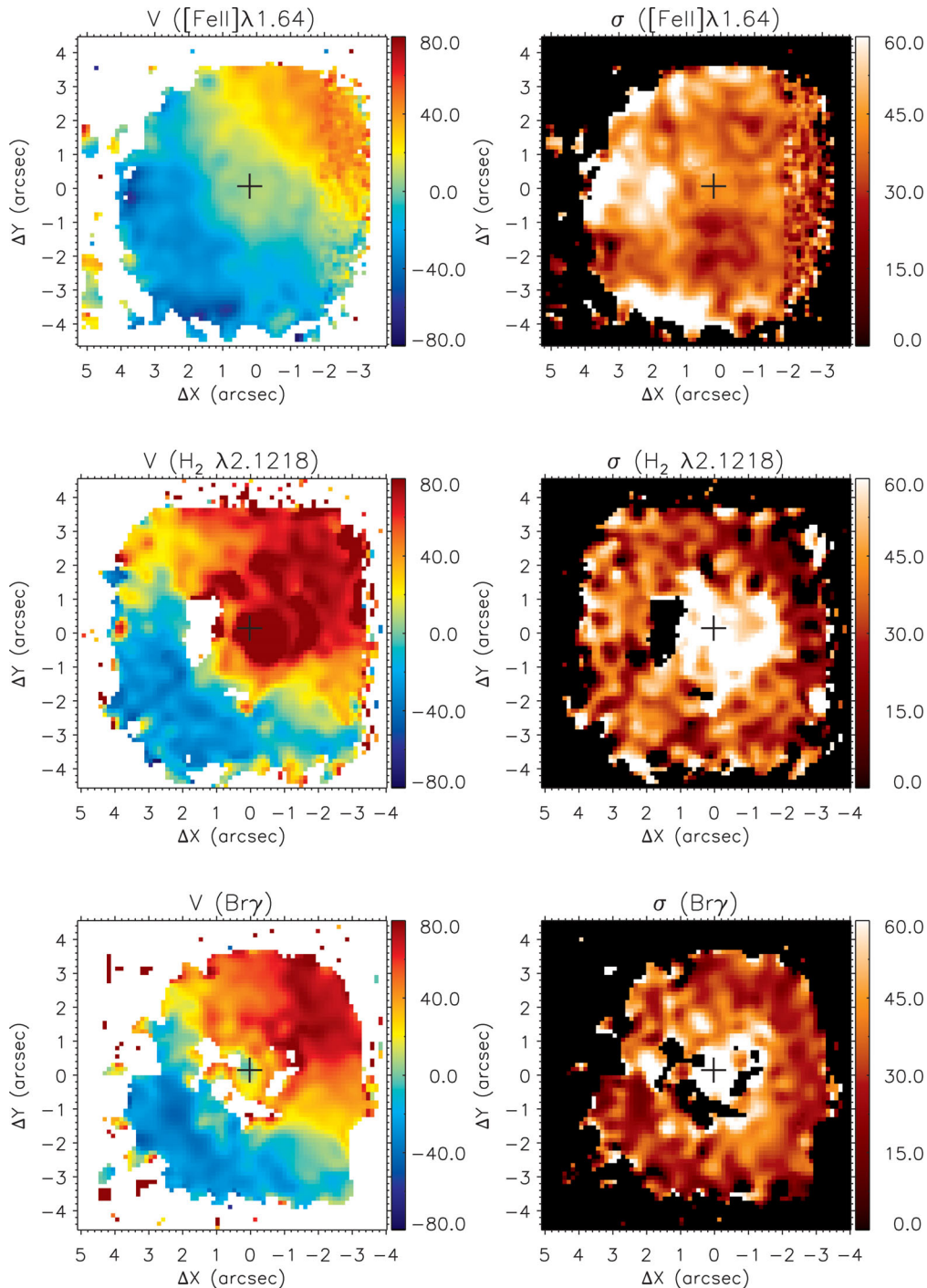


Figure 7. UV *HST* image of NGC 4303 previously discussed by Colina et al. (2002).

only 60 km s^{-1} . The [Fe II] map shows the highest values to the east and south-south-east of the nucleus and the H_2 and $\text{Br}\gamma$ present the highest values at the nucleus. The uncertainties in σ and velocity are smaller than 15 km s^{-1} for all emission lines at most locations. For the nucleus, the uncertainties for the H_2 and $\text{Br}\gamma$ are larger due to the low snr for these lines, with typical uncertainties of 25 km s^{-1} . Uncertainties of about 20 km s^{-1} are observed for the [Fe II] at locations between 2 and 3 arcsec west (right side of the FoV) due to a lower exposure time at these locations (effect of the spatial dithering).

4 DISCUSSION

4.1 (Circum)nuclear stellar and gas distribution: from spirals to ring structure?

UV and near-IR *Hubble Space Telescope* (*HST*) images of NGC 4303 show a nuclear spiral with several knots of star-forming clusters, as seen in Fig. 7, and a weak nuclear stellar bar (Colina & Wada 2000), respectively. The nuclear spiral is not evident in the near-IR emission-line flux distributions shown in Fig. 2, where the structure observed can be better described as a ring of CNSFRs with

radius of about 2.5–3.2 arcsec (200–250 pc). The CNSFRs seem to correspond to complexes of the strongest star-forming clusters observed in the UV *HST* image. This ring is coincident with the inner Lindblad resonance, as derived by Schinnerer et al. (2002) from the observations of the CO cold molecular gas, explaining why the gas has accumulated in the ring, giving origin to the star clusters.

The emission-line flux distributions presented in Fig. 2 show distinct structures for the different emission lines. The strongest emission for the [Fe II] and H₂ lines is from the nucleus, while the hydrogen recombination lines show emission predominately from the CNSFRs. The [Fe II] shows an elongation to ≈ 1.5 arcsec (120 pc) north-east, where an outflow has been observed in [O III] line emission (Colina & Arribas 1999). No emission associated with this outflow is observed in the H₂ map, probably due to the dissociation of the H₂ molecule by the AGN emission, as commonly seen for Seyfert galaxies (e.g. Storchi-Bergmann et al. 2009; Riffel et al. 2014). The nuclear H₂ emission shows instead an elongation towards the west, the same orientation observed in the cold molecular gas emission, connecting the nucleus with the circumnuclear ring (Schinnerer et al. 2002).

In the ring, although the flux distribution in [Fe II] is similar to those of the hydrogen recombination lines, the brightest Pa β and Br γ regions (A and B) are located south-west of the nucleus, while for [Fe II] the brightest region is an unresolved knot (F) to the south-east. This difference is consistent with the scenario in which regions A and B are younger than region F, which has stronger [Fe II] emission due excitation by shocks from SNe, contributing more at a later age (see discussion below).

The hot H₂ emission is strongest in the east part of the ring, at locations that seem to be anti-correlated with the locations of strongest Pa β , Br γ and [Fe II] emission, that coincide also with the UV knots of recent SF. In previous studies by our group (e.g. Storchi-Bergmann et al. 2009), we concluded that the temperature of the region emitting hot H₂ is ≈ 2000 K, and that the excitation mechanism was thermal, as a result of heating by either X-rays from AGN or shocks from both AGN or SNe. In the ring, the eastern H₂ knots of emission probably originate in regions that are even older than the eastern knot that emits [Fe II] and Br γ lines. These regions would still be hot enough to produce H₂ but not enough to produce Br γ and [Fe II] emission (that require 10 000–15 000 K).

Finally, the *K*-band image in Fig. 2 shows a small elongation to the north-east and south-west, visible in the second isocontour which is similar to that observed in the higher resolution *HST* image (Colina & Wada 2000) and attributed to a weak nuclear stellar bar.

4.1.1 The origin of the nuclear emission

The origin of the nuclear gas emission in NGC 4303 is still an open question, but previous works have suggested that the ionizing source is a combination of a low-luminosity AGN and a young massive stellar cluster (Colina et al. 1997, 2002; Colina & Arribas 1999).

The near-IR emission-line ratios can be used to further investigate this point. The line-ratio values from the nucleus can also be compared with those from the CNSFRs. For the nucleus, we obtain $H_2/Br\gamma = 1.4 \pm 1.2$ and $[Fe II]\lambda 1.64/Br\gamma = 3.6 \pm 2.8$ using the values listed in Table 1. These values are typical of Seyfert nuclei, but also of excitation by shocks from SNe (Reunanen et al. 2002; Rodríguez-Ardila et al. 2004, 2005; Colina et al. 2015). They are also significantly higher than those observed in the ring, for example, from regions A and B ($H_2/Br\gamma \sim 0.4$ and $[Fe II]\lambda 1.64/Br\gamma \sim 1.0$) where the presence of young (2.5–7.5 Myr)

clusters dominating the ionization is well established from UV spectroscopy (Colina et al. 2002). Thus, the near-IR diagnostics also suggest the presence of an AGN at the nucleus, confirming previous results that the nuclear emission has a composite nature. Alternatively, an SN-dominated 8–40 Myr star-forming cluster could produce such enhanced line ratios, but there is no evidence so far of a cluster with this age at the nucleus, only of a younger one (≈ 4 Myr old). Moreover, the fact that the [Fe II] emission at the nucleus is extended along the ionized [O III] outflow suggests that the nuclear emission of [Fe II] and the H₂ could be mainly due to X-rays emitted by the AGN (Jiménez-Bailón et al. 2003) and/or shocks in the outflow.

4.1.2 The circumnuclear star-forming regions

Colina et al. (1997) reported the presence of a circumnuclear spiral structure with several UV-bright knots identified as young (few Myr old) star-forming regions (Colina & Arribas 1999). The CNSFRs observed in the flux maps of Fig. 2 and EqW maps of Fig. 4 show a structure similar to that seen in the UV continuum and optical emission-line flux maps (Colina & Arribas 1999), but with a ring rather than a spiral structure. [We note that the region identified as A in Fig. 4 corresponds to regions G and F of Colina et al. (1997).] As discussed in Section 4.1, the location of the ring agrees with that of the inner Lindblad resonance and therefore it may be a stable structure.

Assuming that the CNSFR ring is circular and located in the plane of the galaxy, we can use the observed geometry to derive the inclination of the ring relative to the plane of the sky. In the Br γ EqW map (Fig. 4), the CNSFR shows an elliptical shape with major axis of $a \sim 6$ arcsec oriented along PA $\approx 135^\circ$ and a minor axis of $b \sim 5$ arcsec. The resulting inclination of the ring is $i = \arccos(b/a) \approx 33^\circ$, which is similar to the inclination of large-scale disc of NGC 4303 ($i \approx 27^\circ$).

The H₂/Br γ and [Fe II]/Br γ maps show small values in the CNSFR (see Fig. 3). [Fe II]/Br γ is smaller than 2 for all star-forming regions, being consistent with values expected for young stellar clusters (Colina et al. 2015). The H₂/Br γ ratio for most star-forming regions is smaller than 0.6, as expected for a young cluster, with exception of the regions G and H (identified in Fig. 4) with higher values (of ~ 1), suggesting an additional mechanism for the excitation of the H₂ emission there, such as shocks from SN explosions or diffuse X-ray emission heating the gas and exciting the H₂ molecule.

The integrated emission-line fluxes given in Table 1 have been used to derive a number of physical properties of the star-forming clumps in the CNSFR that are listed in Table 2, as follows. The values of the rate of ionizing photons $Q[H^+]$ and star formation rate (SFR) were derived under the assumptions of continuous SF, and should be considered only a proxy of these parameters.

The emission rate of ionizing photons for each star-forming region was obtained following Riffel et al. (2009), using

$$\left(\frac{Q[H^+]}{s^{-1}}\right) = 7.47 \times 10^{13} \left(\frac{L_{Br\gamma}}{\text{erg s}^{-1}}\right) \quad (1)$$

and the star formation rate (SFR) using (Kennicutt 1998)

$$\left(\frac{\text{SFR}}{M_\odot \text{ yr}^{-1}}\right) = 8.2 \times 10^{-40} \left(\frac{L_{Br\gamma}}{\text{erg s}^{-1}}\right), \quad (2)$$

where $L_{Br\gamma}$ is the Br γ luminosity, under the assumption of continuous rate.

In order to estimate the mass of stars of each CNSFR, we need to assume an age for the region. Detailed spectral energy distribution (SED) fitting of the *HST* UV spectra of the nucleus and of the

Table 2. Physical parameters of the CNSFRs in NGC 4303. The location of each region is indicated in Fig. 4. $Q[\text{H}^+]$: ionizing photons rate, SFR: equivalent star formation rate under the assumption of continuous SF following Kennicutt (1998), M : mass of the cluster assuming a cluster instantaneously formed with age 4 Myr, M_{HII} : mass of ionized gas, M_{H_2} : mass of hot molecular gas, σ_l : velocity dispersion for the line l .

Region	N	A	B	C	D	E	F	G	H
$\log Q[\text{H}^+] (\text{s}^{-1})$	51.1 ± 0.12	51.2 ± 0.02	51.3 ± 0.02	50.9 ± 0.02	50.8 ± 0.03	50.7 ± 0.03	50.8 ± 0.03	50.6 ± 0.03	50.6 ± 0.04
$\text{SFR} (10^{-2} M_{\odot} \text{ yr}^{-1})$	1.3 ± 0.31	1.8 ± 0.07	2.0 ± 0.09	0.8 ± 0.04	0.7 ± 0.04	0.6 ± 0.04	0.7 ± 0.04	0.5 ± 0.03	0.4 ± 0.03
$M (10^5 M_{\odot})$	1.0 ± 0.30	1.3 ± 0.06	1.5 ± 0.06	0.6 ± 0.03	0.5 ± 0.03	0.4 ± 0.03	0.5 ± 0.04	0.4 ± 0.02	0.3 ± 0.02
$M_{\text{HII}} (10^3 M_{\odot})$	8.2 ± 1.9	11.1 ± 0.4	12.4 ± 0.5	5.1 ± 0.3	4.0 ± 0.3	3.7 ± 0.2	4.4 ± 0.3	2.9 ± 0.2	2.5 ± 0.2
$M_{\text{H}_2} (M_{\odot})$	9.8 ± 1.6	4.7 ± 0.3	4.4 ± 0.3	2.0 ± 0.2	2.5 ± 0.2	2.4 ± 0.1	1.7 ± 0.2	2.9 ± 0.1	2.4 ± 0.2
$\sigma_{\text{FeII}} (\text{km s}^{-1})$	44.6 ± 10.4	40.1 ± 6.1	37.9 ± 6.7	44.3 ± 9.2	45.5 ± 9.2	49.5 ± 10.3	52.9 ± 6.5	43.2 ± 6.1	58.9 ± 9.6
$\sigma_{\text{H}_2} (\text{km s}^{-1})$	80.2 ± 16.2	49.6 ± 5.5	39.1 ± 4.7	40.0 ± 7.3	36.7 ± 4.4	36.7 ± 3.6	43.8 ± 7.3	43.5 ± 3.1	39.3 ± 4.6
$\sigma_{\text{Br}\gamma} (\text{km s}^{-1})$	81.8 ± 23.7	40.4 ± 2.6	32.3 ± 2.5	33.7 ± 3.0	32.8 ± 3.9	33.7 ± 3.9	30.9 ± 3.5	34.2 ± 3.6	29.3 ± 4.6

two brightest UV circumnuclear regions (Colina et al. 2002) led to the conclusion that they are best reproduced by instantaneous star-forming bursts of age about 4 Myr. This age was thus used to estimate the mass of each region under the assumption of instantaneous SF using the `STARBURST 99` code (Leitherer et al. 1999, 2010, 2014; Vazquez & Leitherer 2005) and assuming the same initial mass function (IMF) parameters as in Colina et al. (2002) – i.e. a Salpeter IMF, with mass of the stars between 1 and 100 M_{\odot} and solar metallicity. Considering these parameters, a 4 Myr old cluster with mass $1 \times 10^5 M_{\odot}$ will produce a rate of ionizing photons (<13.6 eV) of $\log Q_M \sim 51.1$ photons s^{-1} . Therefore, the mass of the young star-forming regions can be obtained from the observed $\log Q$ listed in Table 2 as $M = 1 \times 10^5 M_{\odot} Q/Q_M$. The resulting masses for the clusters are shown in Table 2 and are in the range $0.30\text{--}1.45 \times 10^5 M_{\odot}$. For more evolved regions (e.g. with ages ~ 10 Myr old instead of 4 Myr), the masses will increase by a factor of 100 as the ionizing radiation is a steep function of age for an instantaneous burst.

The mass of ionized (M_{HII}) gas can be derived as (e.g. Osterbrock & Ferland 2006; Storchi-Bergmann et al. 2009)

$$\left(\frac{M_{\text{HII}}}{M_{\odot}}\right) = 3 \times 10^{19} \left(\frac{F_{\text{Br}\gamma}}{\text{erg cm}^{-2} \text{ s}^{-1}}\right) \left(\frac{D}{\text{Mpc}}\right)^2 \left(\frac{N_e}{\text{cm}^{-3}}\right)^{-1}, \quad (3)$$

where D is the distance to the galaxy, $F_{\text{Br}\gamma}$ is the $\text{Br}\gamma$ flux and N_e is the electron density. We have assumed an electron temperature of 10^4 K and density of $N_e = 500 \text{ cm}^{-3}$. The mass of hot molecular gas is estimated using (e.g. Scoville et al. 1982; Riffel et al. 2008, 2014)

$$\left(\frac{M_{\text{H}_2}}{M_{\odot}}\right) = 5.0776 \times 10^{13} \left(\frac{F_{\text{H}_2\lambda 2.1218}}{\text{erg s}^{-1} \text{ cm}^{-2}}\right) \left(\frac{D}{\text{Mpc}}\right)^2, \quad (4)$$

where $F_{\text{H}_2\lambda 2.1218}$ is the H_2 ($2.1218 \mu\text{m}$) emission-line flux, and the assumptions of local thermal equilibrium and excitation temperature of 2000 K were used.

The resulting values of the ionized and hot molecular gas masses for the nucleus and for each CNSFR are also listed in Table 2. In summary, assuming a typical age of about 4 Myr for the star-forming clumps, the stellar masses in young stars are in the range $3\text{--}10 \times 10^4 M_{\odot}$, the ionized gas mass is about 10 times lower and the mass of hot molecular gas is in the range $3\text{--}4 \times 10^{-5} M_{\odot}$. The ratios between the masses of ionized and hot molecular gas are between 1000 and 2800, with the lower ratios observed for the regions G and H. For the nucleus, $M_{\text{HII}}/M_{\text{H}_2} \approx 830$. These ratios are similar to those in the central region of Seyfert galaxies (e.g. Storchi-Bergmann et al. 2009; Riffel et al. 2014), although distinct scenarios are expected for the heating of the gas. In AGNs, the H_2

emission is usually due to thermal processes, i.e. heating of the gas by shocks or X-rays from the AGN, while for the CNSFRs, young stars play an important role in the excitation of the H_2 . Finally, the $Q[\text{H}^+]$ and equivalent SFR derived for the CNSFR of NGC 4303 are in good agreement with those obtained for other CNSFRs in nearby galaxies characterized by a moderate star-forming regime (e.g. Shi, Gu & Peng 2006; Wold & Galliano 2006; Dors et al. 2008; Galliano & Alloin 2008; Falc3n-Barroso et al. 2014).

4.1.3 The $[\text{Fe II}]/\text{Br}\gamma$ versus $\text{H}_2/\text{Br}\gamma$ diagnostic diagram

In order to better study the gas excitation, we constructed the $[\text{Fe II}]/\text{Br}\gamma$ versus $\text{H}_2/\text{Br}\gamma$ diagnostic diagram shown in Fig. 8. This diagram shows a big overlap of regions corresponding to SNe and AGN, as some excitation processes, like shocks and thermal heating, are common to both AGN and SN. The black dots correspond to all observed spaxels and are mostly located in the region of SNe and/or AGN, with some points covering part of the SF region. This behaviour is typical of luminous star-forming infrared galaxies and

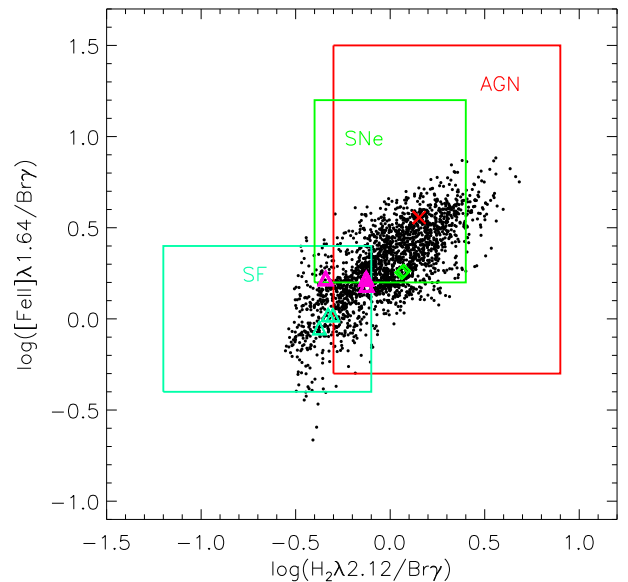


Figure 8. $[\text{Fe II}] \lambda 1.64 \mu\text{m}/\text{Br}\gamma$ versus $\text{H}_2 \lambda 2.12 \mu\text{m}/\text{Br}\gamma$ diagnostic diagram for the central region of NGC 4303. The black points correspond to all the spaxels for which we were able to measure both line ratios. The red cross represents the nucleus, the green diamonds are for regions G and H and the pink/blue triangles represent the ratios for regions D to F (A to C), as labelled in Fig. 4. The limits corresponding to excitation by young stars (SF), SN remnants and AGN are from Colina et al. (2015).

interpreted as due to excitation by combined effects of the AGN and stellar ionizing radiation plus shocks in AGN outflows, stellar winds and SN explosions (Colina et al. 2015).

For the nucleus, the line ratios are high and typical of AGNs, while for the brightest regions in the UV (A to C) in the CNSFR, which are the youngest (see discussion below), the line ratios are typical of star-forming regions. The older star-forming regions in the CNSFR (D to H) are displaced towards the SN region, with regions G and H presenting the most extreme ratios, likely associated with SN explosions. The line ratios are thus compatible with an age difference between the east (older) and west (younger) side of the ring (see Section 4.1.4 for further discussion).

4.1.4 How does the SF proceed in the nucleus and CNSFRs ring?

The SF in the nuclear regions of early-type spirals frequently occurs in ring-like structures with radius of 1 kpc or less. Examples include galaxies with luminous AGNs in their centres as well as many others with a weak AGN or star-forming nucleus (Genzel et al. 1995; Storchi-Bergmann, Wilson & Baldwin 1996a; Storchi-Bergmann et al. 1996b; Böker et al. 2008; van der Laan et al. 2013a,b, 2015; Falcón-Barroso et al. 2014). It is well established that bars in galaxies can drive large quantities of gas to the inner regions, accumulating into inner resonances, generating and maintaining subsequent SF there (Combes & Gerin 1985; Buta & Combes 1996; Heller & Shlosman 1996). Two scenarios have been considered so far to explain the SF in circumnuclear rings: the ‘popcorn’ (Elmegreen 1994) and the ‘pearls on a string’ (Böker et al. 2008). As discussed in the introduction, in the ‘popcorn’ scenario the stellar clusters form at random positions with no age sequence, while in the ‘pearls-on-a-string’ scenario, the clusters are formed where the gas enters the rings and then age as they orbit the ring forming a string of ageing clusters.

Some previous studies favour the ‘pearls-on-a-string’ scenario (Böker et al. 2008; Falcón-Barroso et al. 2014), in galaxies with evidence of gas inflow into the ring (van der Laan et al. 2013a). However, there are also rings that appear to be a combination of the two scenarios (van der Laan et al. 2015). An $H\alpha$ imaging survey of 22 galaxies with CNSFRs (Mazzuca et al. 2008) has shown that about half of the rings show azimuthal age gradients as expected in the ‘pearls-on-a-string’ scenario, while the other half show no age pattern, have a flat age distribution, or even a radial gradient. Thus, the SF in the (circum)nuclear regions of galaxies is far from clear.

In order to investigate the best scenario for the circumnuclear SF in NGC 4303, we show in Fig. 9 the sequence of values of the EqW and σ for the H_2 , $Br\gamma$ and $[Fe II]$ emission lines, as well as the corresponding $[Fe II]/Br\gamma$ and $H_2/Br\gamma$ for each CNSFR, labelled from A to H. The top panel shows a small decrease in EqW values for $Br\gamma$, consistent with a small decrease in age from A to H. For the velocity dispersion (middle panel), no clear trend is observed for $Br\gamma$ and H_2 , while for the $[Fe II]$, the σ values show a small increase from regions A to H. This variation is also consistent with a small increase in age from regions A to H, as the presence of SNs in older regions can increase the $[Fe II]$ velocity dispersion. The bottom panel of Fig. 9 shows small positive gradients for both $H_2/Br\gamma$ and $[Fe II]/Br\gamma$ line ratios between regions A and H, and can also be understood as due to an increase in age as shocks from SNe contribute as an additional excitation source for the H_2 and $[Fe II]$ as the regions age, while the evolution of massive stars away from the main sequence diminishes the amount of ionizing radiation, i.e. reducing the flux of $Br\gamma$. This relative age dating is in agreement

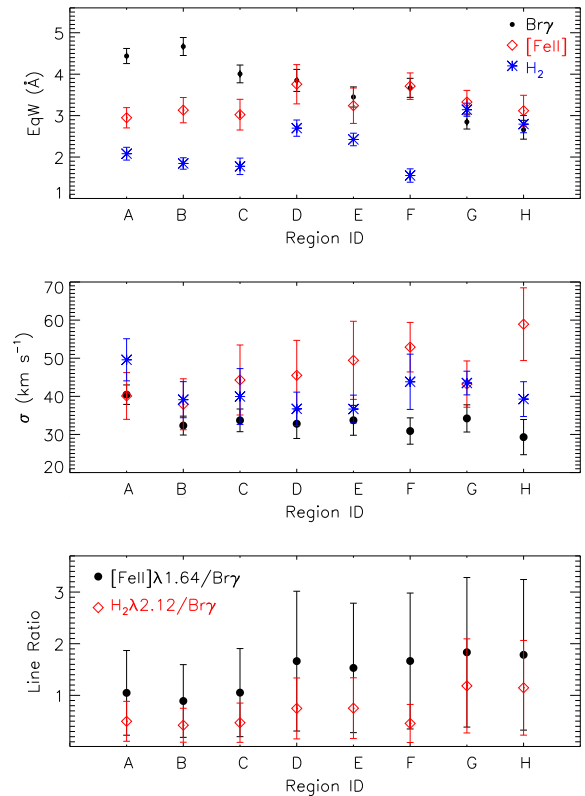


Figure 9. Plots for the EqW (top), σ (middle) and line ratios (bottom) versus region.

with previous conclusions (Colina & Wada 2000; Colina et al. 2002) that identified the east UV knots as older (~ 10 – 25 Myr) than the west knots (~ 2.5 – 7.5 Myr), therefore suggesting an age offset in the star-forming ring. Thus, relative age differences for the star-forming clumps are confirmed from independent tracers in the UV–optical and now the near-IR.

However, although our measurements show a trend suggesting an age sequence along the ring (increasing from A to H), the trend is small and present some ups and downs, being equally consistent just with regions to the east being older than regions to the west. For example, in the case of $H_2/Br\gamma$ instead of a smooth gradient, the observed variation is more consistent with regions G and H being older than the regions A–F. We conclude that the data do not confirm the ‘pearls-on-a-string’ scenario neither the ‘popcorn’ scenario, as there is also no evidence for a random distribution of ages. We can only be sure of an age asymmetry, with the youngest regions to the west and oldest regions to the east.

One interesting new result that can be observed in Fig. 2 is that the regions of strongest H_2 emission in the ring are approximately anti-correlated with the regions of strongest $Br\gamma$ and $[Fe II]$ emission. While the latter coincide with the UV knots of recent SF, the H_2 knots are observed mostly in the east part of the ring, but not coincident with the bright $Br\gamma$ and $[Fe II]$ knot there. In previous results from our group (e.g. Storchi-Bergmann et al. 2009), we concluded that the temperature of the region where hot H_2 is observed is ≈ 2000 K, and that the mechanism producing the hot H_2 emission was thermal excitation as a result of heating either by X-rays from the AGN or shocks from SN. In the ring, the dominant mechanism should be shocks from SN; thus, the eastern knots of H_2 emission

would be hot (2000 K) regions associated with fading SN, being older than the eastern knot of [Fe II] and Br γ emission. These regions would be hot enough to produce H $_2$ but not to produce Br γ and [Fe II] emission (requiring 10 000–15 000 K).

Our results can be compared with those for the cold molecular gas (Schinnerer et al. 2002). The asymmetry in the SF along the ring appears to follow the distribution of cold molecular gas, dominated in mass and surface density by the western spiral and gas lane (Schinnerer et al. 2002). At the resolution of the CO observations (2 arcsec), the large concentration of molecular gas in the spiral seems to be located just outside the CNSFR, suggesting therefore not a direct correspondence between the regions where the SF is taking place now and the regions with the highest molecular gas densities (fig. 10 in Schinnerer et al. 2002). In addition, the east side of the ring appears to be forming very few stars now (as judged from the Br γ and UV emission), and is almost devoid of cold molecular gas, in particular the north-east region (Schinnerer et al. 2002). On the other hand, this is one of the regions where there is enhanced emission from hot molecular gas. Thus, molecular gas seems to exist there, but is heated by local SN, as discussed in the previous paragraph. In summary, regarding the cold molecular gas distribution, while there is a similar distribution with the youngest star-forming regions globally around the ring, this does not seem to occur on scales of a few pc.

The CNSFR is made up of small flocculent spirals or filament-like structures breaking into star-forming clumps extending along large sectors (≈ 300 – 400 pc) of the ring (see Fig. 7). This has been interpreted as fragmentation of a gas disc due to gravitational instabilities (Colina & Wada 2000). The fact that the range of estimated ages for the young star-forming regions in the south-west arc of the ring is very small suggests that the fragmentation is taking place quasi-simultaneously (i.e. in less than few Myr) over sectors extending by hundred of parsecs. In addition, the east side of the ring appears to have formed stars some 10–15 Myr before the west side. Again the lack of an obvious age gradient suggests that the SF was essentially simultaneous over a large sector of the ring. In addition, if the ring is rotating around the nucleus as indicated by our stellar and gas kinematic maps – which imply a rotational period of about 10 Myr – a possible scenario is that the oldest stellar clusters were formed in the west side of the ring, but, after 10 Myr, have already almost completed one turn and are now observed in the south-east part of the ring.

4.2 Mass of molecular and ionized gas in the ring

Equations (3) and (4) can be used to calculate the total mass of ionized and hot molecular gas in the inner $9 \text{ arcsec} \times 9 \text{ arcsec}$ of NGC 4303 covered by our FoV. By integrating the spectra over the total FoV and fitting the H $_2$ and Br γ emission-line profiles from the resulting spectrum, we obtain $F_{\text{H}_2 \lambda 2.1218} \sim 1.2 \times 10^{-14} \text{ erg s}^{-1} \text{ cm}^{-2}$ and $F_{\text{Br}\gamma} \sim 8.5 \times 10^{-15} \text{ erg s}^{-1} \text{ cm}^{-2}$. The corresponding masses are $M_{\text{H}_2} \sim 110 M_{\odot}$ and $M_{\text{H II}} \sim 1.9 \times 10^5 M_{\odot}$. Both values are about three times the sum of the masses for the individual star-forming regions, shown in Table 2 and are in good agreement with the values found for the central region of active galaxies (e.g. Riffel et al. 2014, 2015).

However, the M_{H_2} derived above may be just a small fraction of the total mass of molecular gas available in the central region of NGC 4303 as the ratio between cold and hot molecular gas is usually in the range 10^5 – 10^7 (Dale et al. 2005; Müller-Sánchez et al.

2006; Mazzalay et al. 2013). Following Mazzalay et al. (2013), the mass of cold molecular gas can be obtained by

$$\frac{M_{\text{cold}}}{M_{\odot}} \approx 1174 \times \left(\frac{L_{\text{H}_2 \lambda 2.1218}}{L_{\odot}} \right), \quad (5)$$

where $L_{\text{H}_2 \lambda 2.1218}$ is the luminosity of the H $_2$ line. We derive $M_{\text{cold}} \sim 10^8 M_{\odot}$ and of $\sim 6.25 \times 10^6 M_{\odot}$ for the entire CNSFR and for the nucleus (60 pc radius), respectively. This large amount of molecular gas can be used to feed the AGN and/or to form stars. The estimated mass of cold H $_2$ gas for the entire CNSFR is in good agreement with the one obtained directly from CO observations of the nuclear disc of $6.9 \times 10^7 M_{\odot}$, as derived by Schinnerer et al. (2002).

4.3 Stellar and gas kinematics

The stellar velocity field shown in the left-hand panel of Fig. 5 clearly presents a rotational component. In order to obtain relevant physical parameters, we fitted the stellar velocity field by a model of a thin disc, in which the stars have circular orbits in the plane of the galaxy, with velocities given by (Bertola et al. 1991)

$$V(R, \Psi) = V_s + \frac{AR \cos(\Psi - \Psi_0) \sin(i) \cos^p \theta}{R^2 [\sin^2(\Psi - \Psi_0) + \cos^2(i) \cos^2(\Psi - \Psi_0)] + c_0^2 \cos^2(i)^{p/2}}, \quad (6)$$

where R and Ψ are the coordinates of each pixel in the plane of the sky, A is the amplitude of the rotation curve, Ψ_0 is the position angle of the line of nodes, V_s is the systemic velocity, i is the disc inclination relative to the plane of the sky, c_0 is a concentration parameter and p is a model fitting parameter.

During the fit, the kinematical centre was kept fixed at the location of the peak of the continuum emission, and the inclination of the disc was fixed to the inclination of the CNSFR $i = 33^\circ$, obtained in Section 4.1.2. The difference between the observed and modelled velocities is smaller than 10 km s^{-1} at most locations and thus we conclude that the adopted rotating disc model is a good representation of the observed velocity field. The best-fitting model resulted in the following parameters: $V_s = 1567 \pm 17 \text{ km s}^{-1}$, $\Psi_0 = 136^\circ \pm 1^\circ$, $A = 160 \pm 7 \text{ km s}^{-1}$ and $c_0 = 2.3 \pm 0.2 \text{ arcsec}$. Based on optical IFS with a coarser angular resolution and lower spectral resolution, Colina & Arribas (1999) showed that the gas velocity field of NGC 4303 is consistent with a rotating disc with inclination of 45° , distinct from the inclination of the large-scale disc adopted here. Fixing the inclination of the disc to this value, we obtain similar physical parameters, except for the amplitude of the rotation curve that is smaller – $A = 132.1 \pm 5.2 \text{ km s}^{-1}$, but the quality of the fit is worse and thus we decided to adopt the inclination of the large-scale disc.

The stellar velocity dispersion map shows a ring of small values co-spatial with the ring of CNSFRs, showing that the stars still have the ‘cold’ kinematics of the raw gas that formed the stars. These low- σ_* structures have been previously observed for Seyfert galaxies via similar near-IR IFS for which stellar population synthesis has confirmed that these structures are associated with intermediate-age (0.3–0.7 Gyr) stellar populations (e.g. Riffel et al. 2010). In Dametto et al. (in preparation), we will present a detailed study of the optical/near-IR SED and verify the validity of this interpretation. At locations just beyond the CNSFR, the higher σ_* values – ranging from 70 to 100 km s^{-1} , can be attributed to the bulge of the galaxy.

The velocity fields for all emission lines are similar to that presented by Colina & Arribas (1999) on the base of optical observations, presenting a rotation pattern similar to that of the stars. We

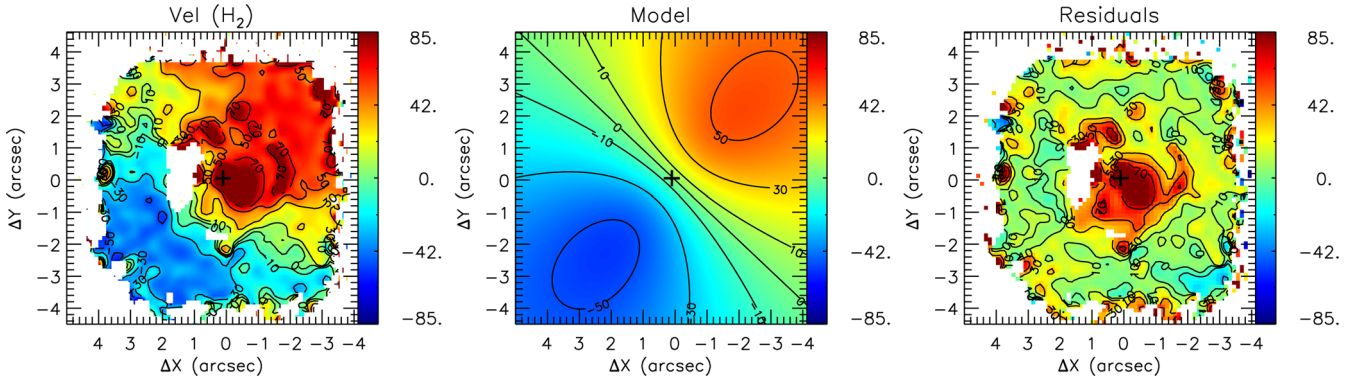


Figure 10. Left: H_2 velocity field; middle: rotating disc model and right: residual map, obtained as the difference of the observed velocities and the model. The colour bars show the velocity in units of km s^{-1} .

fitted the gas velocity field with the same model used to fit the stellar velocity field, keeping fixed all geometric parameters derived for the stars, allowing only the amplitude of the rotation curve to change. We confirm that this model reproduces well the various gas velocity fields, but with a larger velocity amplitude than that observed for the stars: $A = 236 \pm 32 \text{ km s}^{-1}$ for H_2 , $A = 225 \pm 28 \text{ km s}^{-1}$ for $\text{Br}\gamma$ and $A = 151 \pm 25 \text{ km s}^{-1}$ for $[\text{Fe II}]$ (corrected for the inclination of the disc). Distinct rotational velocity amplitudes for the ionized and molecular gas as well as for the stars are commonly observed for active galaxies (e.g. Riffel, Storchi-Bergmann & Winge 2013b; Barbosa et al. 2014), likely indicating a slightly different three-dimensional distribution.

The residuals between the measured and modelled gas velocities were usually smaller than $\approx 10\text{--}20 \text{ km s}^{-1}$, except for the H_2 velocity field shown in Fig. 10. Redshift residuals of $\approx 80\text{--}100 \text{ km s}^{-1}$ are observed in a region extending to $\approx 120 \text{ pc}$ south-west of the nucleus, with similar orientation to that of the nuclear bar, revealing non-circular motions possibly associated with this bar. The velocity dispersion of H_2 is also larger there, suggesting that it may be due to the presence of more than one kinematic component (that our spectral resolution did not allow us to separate). It is interesting to note that a high velocity dispersion was observed also in CO (Schinnerer et al. 2002) in this region, that is identified with a possible molecular gas ‘bridge’ between the ring and the nucleus.

Regarding the ionized gas kinematics, Colina & Arribas (1999) have shown that the optical $[\text{O III}]$ emission shows two components: one due to rotation in the disc and another due to a compact outflow along the minor axis of the galaxy. Although we do not see an outflow in the gas velocity residuals, our data show an increase in the $[\text{Fe II}]$ velocity dispersion to the east-north-east, where the $[\text{Fe II}]$ flux distribution shows an elongation at a similar orientation to that of the $[\text{O III}]$ outflow.

Finally, although the stellar velocity dispersion shows lower velocity dispersion at the ring, the σ maps for the gas (Fig. 6) do not show a decrease or an increase associated with the star-forming regions in the ring. This suggests that the SF is not contributing significantly to the turbulence of the surrounding interstellar medium, as found also for a large sample of low- z Luminous Infrared Galaxies (LIRGs) and Ultra-luminous Infrared Galaxies (ULIRGs) (Arribas et al. 2014) and in high- z galaxies (Genzel et al. 2011). The average velocity dispersion for the ionized gas (traced by the $\text{Br}\gamma$ emission) of the CNSFR of NGC 4303 is $\sigma = 46 \pm 7 \text{ km s}^{-1}$, obtained by fitting the $\text{Br}\gamma$ line profile integrated within a ring with inner radius of 1.5 arcsec and outer radius of 4.0 arcsec, centred at the nucleus. This value is similar to that found for luminous

star-forming clumps ($\sigma = 43 \pm 3 \text{ km s}^{-1}$) of local (U)LIRGs (Arribas et al. 2014). If confirmed for larger samples of galaxies with CNSFR, it would indicate that the velocity dispersion is dominated by global dynamical processes and less affected by local processes like SF on scales of few parsecs.

5 CONCLUSIONS

We have presented new emission-line flux and velocity maps, as well stellar velocity maps of the inner $0.7 \text{ kpc} \times 0.7 \text{ kpc}$ of the nearby spiral galaxy NGC 4303, at spatial resolutions of 78, 47 and 36 pc, for the J , H and K bands, respectively, using near-IR IFS with the VLT instrument SINFONI. The observations cover the nucleus and CNSFR with radius $\approx 200\text{--}250 \text{ pc}$. The main conclusions of this work are as follows.

(i) The near-IR emission-line flux distributions delineate the CNSFR, with emission-line knots in the flux distributions of the different gas phases observed at different locations along the ring. The H_2 and $[\text{Fe II}]$ emission lines show emission peaks at the nucleus, while the H I recombination lines are dominated by emission from the CNSFR;

(ii) Along the ring, the strongest H I and $[\text{Fe II}]$ emission are observed mostly in the west side of the ring and at a region to the south-east, while the strongest emission in H_2 seems to be anti-correlated with them, being observed mostly to the east.

(iii) The properties, $[\text{Fe II}]/\text{Br}\gamma$ and $\text{H}_2/\text{Br}\gamma$ line ratios, EqW and σ of the emission lines along the star-forming ring, support an age difference between the west and east sides of the CNSFR, with the former being younger (2.5–7.5 Myr) than the latter (10–25 Myr).

(iv) The distribution of the star-forming regions and their age differences do not support fully the ‘popcorn’ and the ‘pearls-on-a-string’ scenarios for SF in CNSFRs. The SF in the CNSFR of NGC 4303 appears to be instead episodic with stars forming quasi-simultaneously over a large sector of the ring (covering $\sim 300 \text{ pc}$ along the ring), ageing as they rotate with an orbital time of several Myr.

(v) Assuming that the star-forming regions in the CNSFR are closer to instantaneous bursts with ages of about 4 Myr, we derive masses for the clusters in the range $0.3\text{--}1.5 \times 10^5 M_\odot$. The corresponding masses for the associated ionized and hot molecular gas are about $\sim 0.25\text{--}1.2 \times 10^4$ and $\sim 0.25\text{--}0.5 \times 10^1 M_\odot$, respectively. For stellar populations with older ages of up to 10 Myr, the corresponding stellar masses will increase by up to a factor of 100.

(vi) The [Fe II] emission shows an elongation to ≈ 120 pc north-east of the nucleus that could be associated with the previously known optical ([O III]) outflow.

(vii) The H₂ emission shows an elongation to ≈ 120 pc west of the nucleus that could be the hot counterpart of the already known cold molecular gas ‘bridge’ that connects the nucleus with the large circumnuclear molecular gas reservoir.

(viii) The near-IR emission-line ratios ([Fe II]/Br γ and H₂/Br γ) of the nucleus are consistent with the presence of an AGN and/or an SN-dominated star-forming region. Since there is no evidence for an aged stellar cluster in the nucleus, the line ratios are interpreted as due to the combined effect of X-ray radiation and shocks at the base of the ionization cone of the AGN. Higher angular resolution spectroscopy is required to further explore this scenario.

(ix) The stellar velocity field is well reproduced by a model of a rotating disc with an inclination $i = 33^\circ$ relative to the plane of the sky, major axis oriented along PA $\sim 135^\circ$, and with a velocity amplitude of about 160 km s⁻¹. The stars associated with the CNSFR show smaller velocity dispersion than the surroundings, revealing a cooler dynamical stellar population in the ring, consistent with their recent formation from cold gas.

(x) The gas velocity fields are also dominated by rotation, similar to that observed for the stars but with a larger amplitude. A significant deviation from rotation was observed for the H₂ emission in a region extending ≈ 120 pc to the south-west, along the orientation of the nuclear bar. A higher H₂ velocity dispersion is also observed at this location and is attributed to the presence of more than one kinematic component associated with non-circular motions along the nuclear bar.

All fits files for the emission-line flux distributions, velocity fields and velocity dispersion maps are available online as supplementary material.

ACKNOWLEDGEMENTS

We thank an anonymous referee for useful suggestions which helped to improve the paper. RAR acknowledges support from FAPERGS (project no. 2366-2551/14-0) and CNPq (project no. 470090/2013-8 and 302683/2013-5). LC acknowledges support from CNPq special visitor fellowship PVE 313945/2013-6 under the Brazilian programme Science without Borders. LC, JP and SA are supported by grants AYA2012-32295, AYA2012-39408 and ESP2015-68964 from the Ministerio de Economía y Competitividad of Spain. DAS, RR and TSB thank CNPq for financial support.

REFERENCES

Arribas S., Colina L., Bellocchi E., Maiolino R., Villar-Martín M., 2014, *A&A*, 568, 14
 Barbosa F. K. B., Storchi-Bergmann T., Vale T. B., McGregor P., Riffel R. A., 2014, *MNRAS*, 445, 2353
 Bertola F., Bettoni D., Danziger J., Sadler E., Sparke L., de Zeeuw T., 1991, *ApJ*, 373, 369
 Böker T., Falcón-Barroso J., Schinnerer E., Knapen J. H., Ryder S., 2008, *AJ*, 135, 479
 Buta R., Combes F., 1996, *Fundam. Cosm. Phys.*, 17, 95
 Cappellari M., Emsellem E., 2004, *PASP*, 116, 138
 Cohen M., Wheaton W. A., Megeath S. T., 2003, *AJ*, 126, 1090
 Colina L., Arribas S., 1999, *ApJ*, 524, 637
 Colina L., Wada K., 2000, *ApJ*, 529, 845
 Colina L., García Vargas M. L., Mas-Hesse M., Alberdi A., Krabbe A., 1997, *ApJ*, 484, L41

Colina L., Gonzales Delgado R., Mas-Hesse J. M., Leitherer K., 2002, *ApJ*, 749, 545
 Colina L. et al., 2015, *A&A*, 578, A48
 Combes F., Gerin M., 1985, *A&A*, 150, 327
 Dale D. A., Sheth K., Helou G., Regan M. W., Hüttemeister S., 2005, *ApJ*, 129, 2197
 Davies R. I., Sánchez F. M., Genzel R., Tacconi L. J., Hicks E. K. S., Friedrich S., Sternberg A., 2007, *ApJ*, 671, 1388
 Davies R. I. et al., 2014, *ApJ*, 792, 101
 de Vaucouleurs G., de Vaucouleurs A., Corwin H. G., Jr, Buta R. J., Paturel G., Fouqué P., 1991, *Third Reference Catalogue of Bright Galaxies*. Springer-Verlag, New York
 Diniz M. R., Riffel R. A., Storchi-Bergmann T., Winge C., 2015, *MNRAS*, 453, 1727
 Dors O. L., Storchi-Bergmann T., Riffel R. A., Schmidt A. A., 2008, *A&A*, 482, 59
 Dors O. L., Riffel R. A., Cardaci M. C., Hägele G. F., Krabbe A. C., Pérez-Montero E., Rodrigues I., 2012, *MNRAS*, 422, 252
 Elmegreen B. G., 1994, *ApJ*, 425, L73
 Falcón-Barroso J., Ramos Almeida C., Böker T., Schinnerer E., Knapen J. H., Lancon A., Ryder S., 2014, *MNRAS*, 438, 329
 Fukuda H., Wada K., Habe A., 1998, *MNRAS*, 295, 463
 Galliano E., Alloin D., 2008, *A&A*, 487, 519
 García-Burillo S., Combes F., 2012, *J. Phys.: Conf. Ser.*, 372, 012050
 García-Burillo S., Combes F., Schinnerer E., Boone F., Hunt L. K., 2005, *A&A*, 441, 1011
 Genzel R., Weitzel L., Tacconi-Garman L. E., Blietz M., Cameron M., Krabbe A., Lutz D., Sternberg A., 1995, *ApJ*, 444, 129
 Genzel R. et al., 2011, *ApJ*, 733, 101
 Gonzalez R. C., Woods R. E., 2002, *Digital Image Processing*, 2nd edn. Prentice-Hall, Englewood Cliffs, NJ
 Heller C. H., Shlosman I., 1994, *ApJ*, 424, 84
 Heller C. H., Shlosman I., 1996, *ApJ*, 471, 143
 Hicks E. K. S., Davies R. I., Malkan M. A., Genzel R., Tacconi L. J., Sánchez F. M., Sternberg A., 2009, *ApJ*, 696, 448
 Iserlohe C., Krabbe A., Larkin J. E., Barczys M., McElwain M. W., Quirrenbach A., Weiss J., Wright S. A., 2013, *A&A*, 556, 136
 Jiménez-Bailón E., Santos-Lleó M., Mas-Hesse J. M., Guainazzi M., Colina L., Cerviño M., González Delgado R. M., 2003, *ApJ*, 593, 127
 Kennicutt R. C., 1998, *ARA&A*, 36, 189
 Knapen J. H., Beckman J. E., Heller C. H., Shlosman I., de Jong R. S., *ApJ*, 454, 623
 Koopmann R. A., Kenney J. D. P., Young J., 2001, *ApJS*, 135, 125
 Leitherer C. et al., 1999, *ApJS*, 123, 3
 Leitherer C., Ortiz Otálvaro P. A., Bresolin F., Kudritzki R., Lo Faro B., Pauldrach A. W. A., Pettini M., Rix S. A., 2010, *ApJS*, 189, 309
 Leitherer C., Ekström S., Meynet G., Schaerer D., Agienko K. B., Levesque E. M., 2014, *ApJS*, 212, 14
 Leslie S. K., Kewley L. J., Sanders D. B., Lee N., 2016, *MNRAS*, 455, 82
 Mazzalay X. et al., 2013, *MNRAS*, 428, 2389
 Mazzalay X. et al., 2014, *MNRAS*, 438, 2036
 Mazzuca L. M., Knapen J. H., Veilleux S., Regan M. W., 2008, *ApJS*, 174, 337
 Menezes R. B., da Silva P., Ricci T. V., Steiner J. E., May D., Borges B. W., 2015, *MNRAS*, 450, 369
 Müller-Sánchez F., Davies R. I., Eisenhauer F., Tacconi L. J., Genzel R., Sternberg A., 2006, *A&A*, 454, 492
 Norman N., Scoville N., 1988, *ApJ*, 332, 124
 Osterbrock D. E., Ferland G. J., 2006, *Astrophysics of Gaseous Nebulae and Active Galactic Nuclei*, 2nd edn. University Science Books, Mill Valley, CA
 Reunanen J., Kotilainen J. K., Prieto M. A., 2002, *MNRAS*, 331, 154
 Riffel R. A., 2010, *Ap&SS*, 327, 239
 Riffel R. A., Storchi-Bergmann T., 2011, *MNRAS*, 411, 469
 Riffel R. A., Storchi-Bergmann T., Winge C., McGregor P. J., Beck T., Schmitt H., 2008, *MNRAS*, 385, 1129
 Riffel R. A., Storchi-Bergmann T., Dors O. L., Winge C., 2009, *MNRAS*, 393, 783

- Riffel R. A., Storchi-Bergmann T., Riffel R., Pastoriza M. G., 2010, *ApJ*, 713, 469
- Riffel R., Rodríguez-Ardila A., Aleman I., Brotherton M. S., Pastoriza M. G., Bonatto C., Dors O. L., 2013a, *MNRAS*, 430, 2002
- Riffel R. A., Storchi-Bergmann T., Winge C., 2013b, 430, 2249
- Riffel R. A., Storchi-Bergmann, Vale T. B., McGregor P., 2014, *MNRAS*, 442, 656
- Riffel R. A., Storchi-Bergmann T., Riffel R., 2015, *MNRAS*, 451, 3587
- Rodríguez-Ardila A., Pastoriza M. G., Viegas S., Sigut T. A. A., Pradhan A. K., 2004, *A&A*, 425, 457
- Rodríguez-Ardila A., Riffel R., Pastoriza M. G., 2005, *MNRAS*, 364, 1041
- Schinnerer E., Maciejewski W., Scoville N., Moustakas L. A., 2002, *ApJ*, 575, 826
- Scoville N. Z., Hall D. N. B., Kleinmann S. G., Ridgway S. T., 1982, *ApJ*, 253, 136
- Shi L., Gu Q. S., Peng Z. X., 2006, *A&A*, 450, 15
- Shlosman I., Frank J., Begelman M. C., 1989, *Nature*, 338, 45
- Shlosman I., Begelman M. C., Frank J., 1990, *Nature*, 345, 679
- Skrutskie M. F. et al., 2006, *AJ*, 131, 1163
- Storchi-Bergmann T., Wilson A. S., Baldwin J., 1996a, *ApJ*, 460, 252
- Storchi-Bergmann T., Rodríguez-Ardila A., Schmitt H. R., Wilson A. S., Baldwin J., 1996b, *ApJ*, 472, 83
- Storchi-Bergmann T., McGregor P. J., Riffel R. A., Simões Lopes R., Beck T., Dopita M., 2009, *MNRAS*, 394, 1148
- Storchi-Bergmann T., Lopes R. D., McGregor P. J., Riffel R. A., Beck T., Martini P., 2010, *MNRAS*, 402, 819
- van der Laan T. P. R. et al., 2015, *A&A*, 575, A83
- van der Laan T. P. R., Schinnerer E., Emsellem E., Hunt L. K., McDermid R. M., Liu G., 2013a, *A&A*, 551, A81
- van der Laan T. P. R. et al., 2013b, *A&A*, 556, A98
- Vazquez G. A., Leitherer C., 2005, *ApJ*, 621, 695
- Winge C., Riffel R. A., Storchi-Bergmann T., 2009, *ApJS*, 185, 186
- Wold M., Galliano E., 2006, *MNRAS*, 369, 47
- Wright C. O., Egan M. P., Kraemer K. E., Price S. D., 2003, *AJ*, 125, 359

SUPPORTING INFORMATION

Additional Supporting Information may be found in the online version of this article:

data_paper.tar

(<http://www.mnras.oxfordjournals.org/lookup/suppl/doi:10.1093/mnras/stw1609/-/DC1>).

Please note: Oxford University Press is not responsible for the content or functionality of any supporting materials supplied by the authors. Any queries (other than missing material) should be directed to the corresponding author for the article.

This paper has been typeset from a \TeX/L\AA\TeX file prepared by the author.